

On the Functional Relationship Between Fluorescence and Photochemical Yields in Complex Evergreen Needleleaf Canopies

Andrew J. Maguire^{1,2}, Jan U.H. Eitel^{1,2}, Kevin L. Griffin^{3,4}, Troy S. Magney^{5,6}, Ryan A. Long⁷, Lee A. Vierling^{1,2}, Stephanie C. Schmiege⁴, Jyoti S. Jennewein¹, William A. Weygint^{1,2}, Natalie T. Boelman³, and Sarah G. Bruner⁴

¹Department of Natural Resources and Society, University of Idaho, Moscow, ID, USA

²McCall Outdoor Science School, University of Idaho, McCall, ID, USA

³Department of Earth and Environmental Sciences, Lamont-Doherty Earth Observatory, Columbia University, New York, NY, USA

⁴Department of Ecology, Evolution and Environmental Biology, Columbia University, New York, NY, USA

⁵Department of Plant Sciences, University of California, Davis, CA, USA

⁶Division of Geological and Planetary Sciences, California Institute of Technology, Pasadena, CA, USA

⁷Department of Fish and Wildlife Sciences, University of Idaho, Moscow, ID 83844-1136, USA

Corresponding author: Andrew J. Maguire (amaguire@uidaho.edu)

Key Points:

- Needle-scale observations from forests show a nonlinear, irradiance-dependent relationship between fluorescence and photosystem II yields
- We use the breakpoint in this relationship to distinguish physiological constraints on photosystem II operating efficiency
- We use this relationship to contextualize the apparent linear relationship between fluorescence and carbon uptake at the canopy-scale

This is the author manuscript accepted for publication and has undergone full peer review but has not been through the copyediting, typesetting, pagination and proofreading process, which may lead to differences between this version and the Version of Record. Please cite this article as doi: [10.1029/2020GL087858](https://doi.org/10.1029/2020GL087858)

28 Abstract

29 Recent advancements in understanding remotely sensed solar-induced chlorophyll fluorescence
30 often suggest a linear relationship with gross primary productivity at large spatial scales.
31 However, the quantum yields of fluorescence and photochemistry are not linearly related and this
32 relationship is largely driven by irradiance. This raises questions about the mechanistic basis of
33 observed linearity from complex canopies that experience heterogeneous irradiance regimes at
34 sub-canopy scales. We present empirical, data from two evergreen forest sites that demonstrate a
35 nonlinear relationship between needle-scale observations of steady-state fluorescence yield and
36 photochemical yield under ambient irradiance. We show that accounting for sub-canopy and
37 diurnal patterns of irradiance can help identify the physiological constraints on needle-scale
38 fluorescence at 70-80% accuracy. Our findings are placed in the context of how solar-induced
39 chlorophyll fluorescence observations from spaceborne sensors relate to diurnal variation in
40 canopy-scale physiology.

41 Plain Language Summary

42 Chlorophyll fluorescence is a faint signal emitted by plants that can provide information about
43 photosynthesis and other processes important for plant growth. However, fluorescence is
44 governed by complex chemical reactions that depend on light and it is not linearly related to
45 photosynthetic carbon uptake. Ecosystems with complex canopy structure, such as evergreen
46 needleleaf forests, experience dynamic sunlit and shaded conditions which make fluorescence
47 observations challenging to interpret. However, by accounting for incoming light at fine spatial
48 scales in studies using fluorescence, we can track the conditions under which canopies are
49 partitioned by light-saturated and light-limited physiological constraints at 70-80% accuracy.
50 Findings from our field-based study are relevant for interpreting satellite-based measurements of
51 fluorescence as a proxy of photosynthetic carbon uptake. Furthermore, our study underscores the
52 need for further research on how data from leaf-scale studies can be scaled up to shed light on
53 ecosystem responses to changing climatic conditions.

54 1 Introduction

55 Advancements in measuring chlorophyll fluorescence (ChlF), particularly retrievals of
56 solar-induced fluorescence (SIF) from satellite instruments, have led to improvements in
57 understanding sensitivity of the terrestrial carbon cycle to environmental conditions (Guanter et
58 al., 2014; Xing Li et al., 2018; Magney, Bowling, et al., 2019; Sun et al., 2017). Fluorescence is
59 physically linked to the light reactions of photosynthesis (Alonso et al., 2017; Gu et al., 2019)
60 and is sensitive to the quantity of light absorbed by foliage (i.e., absorbed photosynthetically
61 active radiation, APAR) and to the efficiency which this light is used to drive photochemical
62 processes (e.g., the quantum yield of photosystem II (Φ_{PSII}) and steady-state fluorescence yield
63 (F_t)). SIF has proven useful for tracking seasonal dynamics of canopy physiology in evergreen
64 needleleaf forests (ENFs) (Magney, Bowling, et al., 2019; Walther et al., 2016), for which
65 traditional greenness indices – sensitive to turnover in leaf area and chlorophyll content – have
66 limited value (Jeong et al., 2017). Yet, major uncertainties remain in deciphering the
67 physiological constraints on Φ_{PSII} from SIF (Magney, Bowling, et al., 2019). Pulse amplitude
68 modulated (PAM) fluorometry can be used to actively measure quantum yields (Baker, 2008)
69 which remains challenging from passive SIF observations (Magney et al., 2017). Photochemistry
70 is governed by intrinsic (e.g., genotypic) and extrinsic (e.g., nutrient availability; water,
71 temperature, and radiation stress) controls (Baker, 2008; Krause & Weis, 1991; Maxwell &

72 Johnson, 2000). However, over short-time scales two competing processes are primarily
73 responsible for shaping the $\text{ChlF} - \Phi_{\text{PSII}}$ relationship. Under saturating irradiance, Φ_{PSII} is low and
74 F_t is limited by nonphotochemical quenching (NPQ-limited) – manifesting as dissipation of
75 excess APAR as heat – which induces a positive relationship between Φ_{PSII} and F_t . Under non-
76 saturating irradiance, NPQ is suppressed and F_t is limited by photochemical quenching (PQ-
77 limited), which induces a negative relationship between Φ_{PSII} and F_t (Baker, 2008; Maxwell &
78 Johnson, 2000; Porcar-Castell et al., 2014).

79 The complex canopy structure of ENFs leads to dynamic mosaics of highly illuminated
80 and deeply shaded foliage at a sub-canopy scale, which in turn trigger within-canopy partitioning
81 of NPQ and PQ, respectively. Remotely sensed data from ENFs thus represent an integration of
82 the physiological responses to these aggregated irradiance conditions (Hilker, Coops, Hall, et al.,
83 2008). Previous studies have demonstrated that high-resolution canopy structure measurements
84 (e.g., from lidar) can help characterize heterogeneity in irradiance and constrain estimates of
85 physiological responses at sub-canopy scales (Hall et al., 2008; Hilker et al., 2010; Hilker,
86 Coops, Schwalm, et al., 2008; Middleton et al., 2009). Numerous studies have documented an
87 apparent positive linear relationship between SIF and gross primary productivity (GPP) at
88 canopy-to-landscape scales (Guanter et al., 2014; Xing Li et al., 2018; Sun et al., 2017),
89 suggesting that NPQ is the dominant limitation. Prevalence of PQ-limitation has been linked to
90 departures from linearity in the SIF—GPP relationship, especially in short-term studies that
91 control for seasonal variation (Porcar-Castell et al., 2014; van der Tol et al., 2014; Wieneke et
92 al., 2018). However, there is a lack of empirical evidence from field studies in ENFs that provide
93 mechanistic support for integrated canopy-scale NPQ- and PQ-limitation.

94 Empirical evidence from a needle-scale field experiment revealed a nonlinear relationship
95 between Φ_{PSII} and F_t (Porcar-Castell et al., 2008, 2014). Because of this nonlinearity, F_t cannot
96 be interpreted as a direct proxy of photosynthetic light use efficiency (GPP/APAR) without
97 additional information. Similarly, laboratory studies on *Gossypium* sp. (van der Tol et al., 2014)
98 and *Acer palmatum* leaves (Magney et al., 2017) provided evidence that the sign of slope of the
99 relationship between Φ_{PSII} and F_t is largely dependent on the intensity of irradiance. These
100 findings encourage further investigation of the dynamics and drivers of this relationship in ENF
101 foliage under ambient irradiance. The transferability of this relationship, including how it
102 changes from leaf- to canopy-scales and the threshold at which this sign change occurs, must be
103 determined empirically (Magney et al., 2017; Magney, Frankenberg, et al., 2019; Raczka et al.,
104 2019; Wen et al., 2020). This is important for understanding the physiological differences
105 between processes driven by the light reactions of photosynthesis (F_t , SIF, and Φ_{PSII}) and
106 processes driven by the dark reactions of photosynthesis (GPP) (Damm et al., 2010; Frankenberg
107 & Berry, 2018; Gu et al., 2019). Furthermore, whereas F_t and Φ_{PSII} are quantum yield terms, SIF
108 and GPP are strongly linked by their common driver – APAR by chlorophyll. Therefore,
109 interpreting SIF as a proxy of GPP requires accounting for APAR, which is challenging to
110 quantify (Frankenberg & Berry, 2018) especially in complex canopies.

111 Because most current spaceborne SIF retrievals have fixed diurnal overpass times, studies
112 reliant on such data cannot fully account for canopy irradiance dynamics. Mechanistically, it is
113 likely that NPQ is the limiting factor in early afternoon spaceborne SIF retrievals (e.g.,
114 TROPOMI, OCO-2, and GOSAT), because the observations occur near peak diurnal irradiance
115 when canopy self-shading is minimized. However, even if this is true, questions remain as to
116 whether regularly timed ‘snapshots’ are representative of the physiological state of vegetation
117 within the field of view (Magney, Frankenberg, et al., 2019; Parazoo et al., 2019). Research

118 accounting for how variation in canopy illumination induces physiological regulation of
119 photochemical processes has been limited to modeling studies (Celesti et al., 2018; van der Tol,
120 Verhoef, & Rosema, 2009; van der Tol, Verhoef, Timmermans, et al., 2009) and controlled lab
121 experiments (van der Tol et al., 2014). Diurnally variable (e.g., OCO-3) (Eldering et al., 2019)
122 and continuous (e.g., GeoCARB) (Moore III et al., 2018) observations of spaceborne SIF will
123 provide an opportunity to investigate this effect at large-scales. First, however, it will be critical
124 to leverage PAM fluorometry to understand the conditions under which the relationships among
125 SIF, GPP, F_t , and Φ_{PSII} diverge.

126 We present empirical, field-based needle-scale observations of PAM ChlF from two
127 shade-tolerant ENF species under ambient irradiance. We collected data over a constrained time
128 period to minimize seasonal effects on Φ_{PSII} and F_t (e.g., changes in pigment content). We
129 hypothesized that we would observe a nonlinear relationship between Φ_{PSII} and F_t , that the
130 position of the breakpoint in this relationship (i.e., the threshold in Φ_{PSII} at which the relationship
131 changes sign, signifying a transition between NPQ- and PQ-limitation) would converge with that
132 of prior studies (Magney et al., 2017; Porcar-Castell et al., 2014; van der Tol et al., 2014) at Φ_{PSII}
133 = 0.6, and that the breakpoint would be driven by irradiance. To test these hypotheses we
134 developed a simple model for predicting relative photochemical yield at a sub-canopy scale. We
135 discuss whether this mechanistic model can aid interpretation of large-scale SIF observations
136 from complex canopies experiencing dynamic shading regimes.

137 2 Materials and Methods

138 We implemented a novel experimental framework integrating observations of PAM ChlF
139 with contemporaneous lidar-informed estimates of sub-canopy illumination regimes, the latter of
140 which we validated with *in situ* observations. We then developed a simple model to predict
141 relative Φ_{PSII} using F_t and irradiance.

142 2.1 Study sites

143 Field data were collected at two evergreen needleleaf sites: the forest-tundra ecotone near
144 the Dalton Highway, Alaska, USA (67° 59' 41" N, 149° 45' 16" W, 730 m elevation; Eitel *et al.*
145 2019) on July 7-8, 2017 and a montane forest near McCall, Idaho, USA (44° 54' 22" N, 116° 4'
146 0" W, 1595 m elevation) on July 5-6, 2019. The Alaska site is dominated by white spruce (*Picea*
147 *glauca*). The Idaho site has an understory of grand fir (*Abies grandis*) with an overstory of
148 ponderosa pine (*Pinus ponderosa*) and Douglas fir (*Pseudotsuga menziesii*). Average daily
149 temperature during sampling was 18.0° C and 17.0° C for the Alaska and Idaho sites,
150 respectively. Average daily soil moisture during sampling was 0.24 m³ m⁻³ and 0.11 m³ m⁻³ at 10
151 cm depth for the Alaska and Idaho sites, respectively. Sites were not experiencing drought or
152 disturbance during sampling. Sampling occurred during clear-sky conditions such that the
153 canopies experienced a broad range of variability in sunlit-shading patterns across the day. Four
154 groups of needles from outer branches at 1 – 2 m height above ground from each of 36 *P. glauca*
155 study trees ($n = 144$) in Alaska and six groups of needles from each of 10 *A. grandis* study trees
156 ($n = 60$) in Idaho were sampled. To observe a range of variability in illumination, sampling
157 locations were distributed across crown aspects.

159 2.2 Needle-scale chlorophyll fluorescence measurements

160 We measured ChlF using an Optisci OS30p+, a PAM fluorometer employing a red
161 actinic light (Opti-Sciences, Inc. Hudson, New Hampshire, USA) at a saturating light intensity of
162

163 3500 $\mu\text{mol m}^{-2} \text{s}^{-1}$. Sampled needles were marked to enable repeated measurement. Leaf clips
164 used for ChlF measurements were removed between each measurement to allow for foliage to
165 adapt to ambient light. *P. glauca* needles were sampled six times during daylight hours across
166 the two sampling days; *A. grandis* needles were sampled six times during daylight hours on the
167 first day and once again shortly after sunrise on the second day. The ratio of light-adapted
168 variable to maximal fluorescence (F_v/F_m) represents photosystem II yield (Φ_{PSII}) (Genty et al.,
169 1989). Observations of steady-state fluorescence yield (F_t) were normalized to $F_{t,\text{max}}$ following
170 Magney et al. (2017). F_t can be interpreted as a yield because reported values are effectively
171 normalized by the intensity and frequency of the modulating light from the fluorometer which
172 was consistent across samples. These parameters are analogous to commonly derived parameters
173 of SIF studies: $\text{SIF}_{\text{yield}}$ (i.e., F_t) and photosynthetic light use efficiency (i.e., Φ_{PSII} , not accounting
174 for dark reactions) (Porcar-Castell et al., 2014). We excluded observations when raw
175 measurements were too low to interpret, which may have resulted from insufficient foliage in the
176 instrument viewing window. The final dataset included 523 observations from the Alaska site
177 (98% of recorded observations) and 417 observations from the Idaho site (99% of recorded
178 observations).

179 2.3 Remote sensing data for modeling needle-scale irradiance

180
181 In 2011, airborne lidar data (8 points m^{-2}) were acquired over a 6 km x 1.5 km footprint
182 (Hubbard et al., 2011), covering the extent of the *in situ* ChlF sampling locations in Alaska. We
183 assumed that this lidar survey represented canopy structure at the time of ChlF sampling due to
184 slow vegetation growth rates among high latitude spruce trees (Gamache & Payette, 2004).

185 Contemporaneous with field sampling in Idaho, terrestrial lidar data (> 1 point cm^{-2} ; 0.1
186 mrad beam divergence) were collected for a 150 m x 150 m footprint covering ChlF sampling
187 locations and surrounding vegetation that obscured direct solar exposure. Sampled needles were
188 labeled such that coordinates could be visually determined at sub-centimeter precision from the
189 resulting point cloud.

190 A digital canopy surface model (DSM) of the Alaska site was interpolated from the
191 airborne lidar dataset and gridded at 0.5 m resolution using the R package ‘lidR’ (Roussel et al.,
192 2017). A DSM of the Idaho site was interpolated from the terrestrial lidar dataset and gridded at
193 0.10 m resolution using the R package ‘akima’ (Akima et al., 2016).

194 Sampled trees at the Alaska site were identified using an individual tree detection
195 algorithm implemented in the R package ‘rLiDAR’ (Silva et al., 2017) and validated with field
196 measurements. DSM grid cells collocated with sampled needles were manually selected using
197 canopy height value and directional location within tree crown boundaries. Due to the coarser
198 spatial resolution of the Alaska DSM and the narrow-crowned trees at the forest-tundra ecotone,
199 we were unable to identify unique grid cells corresponding to all sampled needles
200 unambiguously. We limited the sample population to grid cells with canopy height value 1.0-3.0
201 m, as a reasonable approximation of sampling height, and grid cells that could be identified as
202 exclusively corresponding to a given cardinal direction (e.g., sampling locations could not be
203 assigned to unique grid cells for crowns composed of a two-by-two grid cell square). If multiple
204 grid cells fit the aforementioned criteria for a given sampling location, each of these grid cells
205 were selected and the average irradiance value (see section 2.4) was used. Following this
206 approach, coordinates of 89 *P. glauca* sampling locations were approximated.

207 Sampled trees at the Idaho site were identified from labels affixed to tree boles visible in
208 the terrestrial lidar point cloud. Coordinates of sampling locations were extracted by manually

209 selecting terrestrial lidar returns at the fluorometer leaf clip in the point cloud. Coordinates of 60
210 *A. grandis* sampling locations were approximated.

211

212 2.4 Irradiance estimation

213

214 2.4.1 Modeled irradiance

215 We used the R package ‘insol’ (Corripio, 2003, 2015) to model instantaneous irradiance
216 for sampling locations using the DSMs (see section 2.3), geographic location, and atmospheric
217 and surface reflectance parameters, the latter of which were interpolated from satellite remote
218 sensing datasets (Levelt et al., 2006; Mesinger et al., 2006). This approach enabled estimation of
219 direct and diffuse solar irradiance through two steps: (1) top-of-canopy (TOC) direct and diffuse
220 irradiance were calculated based on atmospheric conditions and solar geometry; (2) following
221 previous work exploring light environment effects on spectral reflectance-based indicators of
222 light use efficiency (Hall et al., 2008; Hilker et al., 2010, 2011; Hilker, Coops, Schwalm, et al.,
223 2008; Li & Strahler, 1985), TOC direct irradiance was modulated by canopy surface, accounting
224 for the surface aspect of individual DSM grid cells (based on neighborhood analysis) relative to
225 the normal of the incident solar angle. Next, the DSM was used to simulate shadow casting based
226 on solar geometry. Direct irradiance for grid cells classified as shaded was nullified. Non-zero
227 direct irradiance values were added to TOC diffuse irradiance to yield modeled irradiance for
228 each sampling location.

229

230 2.4.2 Observed irradiance

231 A handheld PYR solar radiation sensor and ProCheck real-time reader (METER, Inc.,
232 Pullman, WA) were used to measure irradiance at sampled *A. grandis* needles from the Idaho
233 site, concurrent with ChlF measurement. The instrument measured incoming radiation across the
234 360 – 1120 nm spectrum, to accuracies within 1 W m^{-2} . *In situ* observations of irradiance were
235 not collected at the Alaska site.

236

237 2.5 Statistical methods

238 We fit mixed-effects models in the ‘lme4’ package in R (Bates et al., 2018) that included
239 irradiance as a fixed effect and sampled needles as a random effect to account for autocorrelation
240 of multiple measurements obtained from the same needles. We used marginal R^2 values
241 (Nakagawa & Schielzeth, 2013) to quantify the degree to which irradiance explained variance in
242 F_t and Φ_{PSII} . To test our first hypothesis of nonlinearity in the relationship between F_t and Φ_{PSII} ,
243 we pooled ChlF observations across sampling periods within each study site and fit both linear
244 regression models and generalized additive models (GAMs) to those data using the ‘mgcv’
245 package in R (Wood, 2019). We compared linear versus nonlinear model fits using adjusted R^2 ,
246 Akaike Information Criterion (AIC), and Akaike weights (w_i) (Burnham & Anderson, 2002). We
247 identified the breakpoint in the relationship between Φ_{PSII} and F_t by determining where the first
248 derivative (i.e., slope) of the GAM equaled zero and the slope switched from positive to
249 negative, based on evidence for this shape by Porcar-Castell et al. (2014) and van der Tol et al.
250 (2014). We then used this breakpoint as a basis for determining the degree to which irradiance
251 alone could be used to parse whether a given observation of F_t corresponded to relatively low
252 Φ_{PSII} (hence NPQ-limited) or relatively high Φ_{PSII} (hence PQ-limited) using generalized linear
253 models with a binomial error distribution.

254 3 Results and Discussion

255 3.1 Variance in Φ_{PSII} driven by irradiance, F_t by NPQ- and PQ-limitation

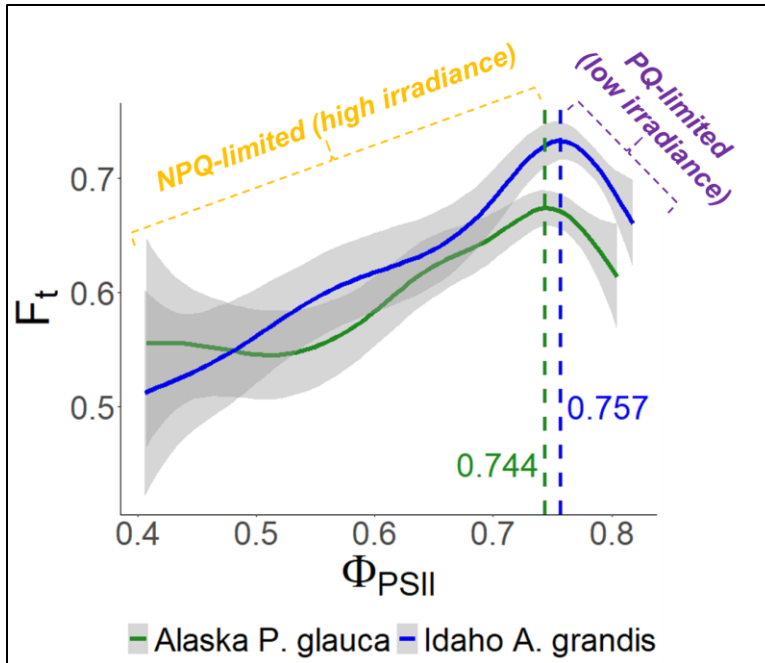
256 Ambient irradiance explained limited variation in F_t (marginal R^2 values were < 0.001
257 and 0.14 for Alaska and Idaho, respectively) whereas it explained considerably more variation in
258 Φ_{PSII} (marginal R^2 values were 0.17 and 0.68 for Alaska and Idaho, respectively). In Idaho,
259 modeled irradiance explained notably less variation in F_t and Φ_{PSII} relative to observed irradiance
260 (marginal $R^2 < 0.01$ and 0.23, respectively). Gu et al. (2019) and van der Tol et al. (2014)
261 presented similar evidence and suggested this disparity is due to photosynthesis saturating at
262 high irradiance whereas absolute fluorescence continues to increase. Among sampled needles in
263 Idaho, both Φ_{PSII} and F_t declined rapidly in response to increased irradiance, implying temporary
264 amplification of NPQ (Porcar-Castell et al., 2006, 2008); such a response was not apparent
265 among sampled needles from the Alaska site (**Fig. S1**). Discrepancies between sites may be
266 attributable to the means by which irradiance was quantified: in Alaska irradiance was modeled
267 whereas in Idaho irradiance was observed. In Idaho, we showed a moderate linear fit between
268 observed and modeled irradiance (slope = 0.51; intercept = 84.53 W m⁻²; RMSE = 271.53 W m⁻²;
269 $r^2 = 0.11$; $p < 0.001$). Error may arise from DSM resolution and inability to account for
270 transmittance through the canopy resulting in mischaracterization of shading at sampling
271 locations (**Fig. S2**).

272

273 3.2 F_t and Φ_{PSII} are nonlinearly related, primarily controlled by irradiance

274 For both study sites, GAMs provided better fits than linear models (Alaska: adjusted $R^2 =$
275 0.10 and 0.08, AIC = -744.76 and -738.478, $w_i = 0.96$ and 0.04; Idaho: adjusted $R^2 = 0.20$ and
276 0.16, AIC = -710.83 and -693.08, $w_i > 0.99$ and < 0.01). The smoothed terms (GAMs) and
277 coefficients (linear models) were significant for both sites ($p < 0.001$). The ratio of w_i values
278 indicated that GAMs were 23.10 and 7171.71 times more likely to be the better fitting models of
279 F_t against Φ_{PSII} . GAMs aligned with the relationships described by Magney et al. (2017), Porcar-
280 Castell et al. (2008, 2014), and van der Tol et al. (2014) and revealed a positive-to-negative sign
281 change in the proportionality of Φ_{PSII} and F_t (**Fig. 1**), supporting our first hypothesis. Despite the
282 site and species differences GAMs from each site converged at their respective Φ_{PSII} breakpoints
283 (Alaska *P. glauca* $\Phi_{\text{PSII}} = 0.744$; Idaho *A. grandis* $\Phi_{\text{PSII}} = 0.757$). This was a notable departure
284 from findings of prior studies which show convergence at $\Phi_{\text{PSII}} = 0.60$ (Magney et al., 2017;
285 Porcar-Castell et al., 2014; van der Tol et al., 2014). That we observed NPQ-limitation across a
286 broader range of Φ_{PSII} relative to prior studies may be related to the shade-tolerance of our study
287 species. Sampling in our study occurred over short timeframes; yet, foliar and whole-plant
288 physiology both respond to seasonal changes in environmental conditions (e.g., nutrient
289 availability, water and temperature stress, and photoperiod). Therefore, future studies should
290 investigate whether the shape of this relationship and the location of the Φ_{PSII} breakpoint changes
291 seasonally and across species and environmental conditions.

292



293 **Figure 1.** Generalized additive models (GAMs) fit to steady-state fluorescence yield (F_t) and
 294 photosystem II yield (Φ_{PSII}) for observations from Alaska *P. glauca* needles (green, $n = 523$) and
 295 Idaho *A. grandis* needles (blue, $n = 417$). 95% confidence intervals are shown in gray.
 296 Breakpoints (dashed lines) were identified as the value of Φ_{PSII} at which the first derivative (i.e.,
 297 slope) equaled zero and the slope switched from positive to negative. Observations of F_t were
 298 normalized to $F_{t,max}$ following Magney et al. (2017).
 299

300
 301 The observed nonlinear relationship between Φ_{PSII} and F_t demonstrates that parameters of
 302 ChlF cannot be interpreted as a direct proxy of photosynthetic status. Where a given observation
 303 falls on this curve is dependent on irradiance (**Fig. 2**), supporting our third hypothesis and
 304 revealing a pathway to discern relative photochemical yield.
 305

306

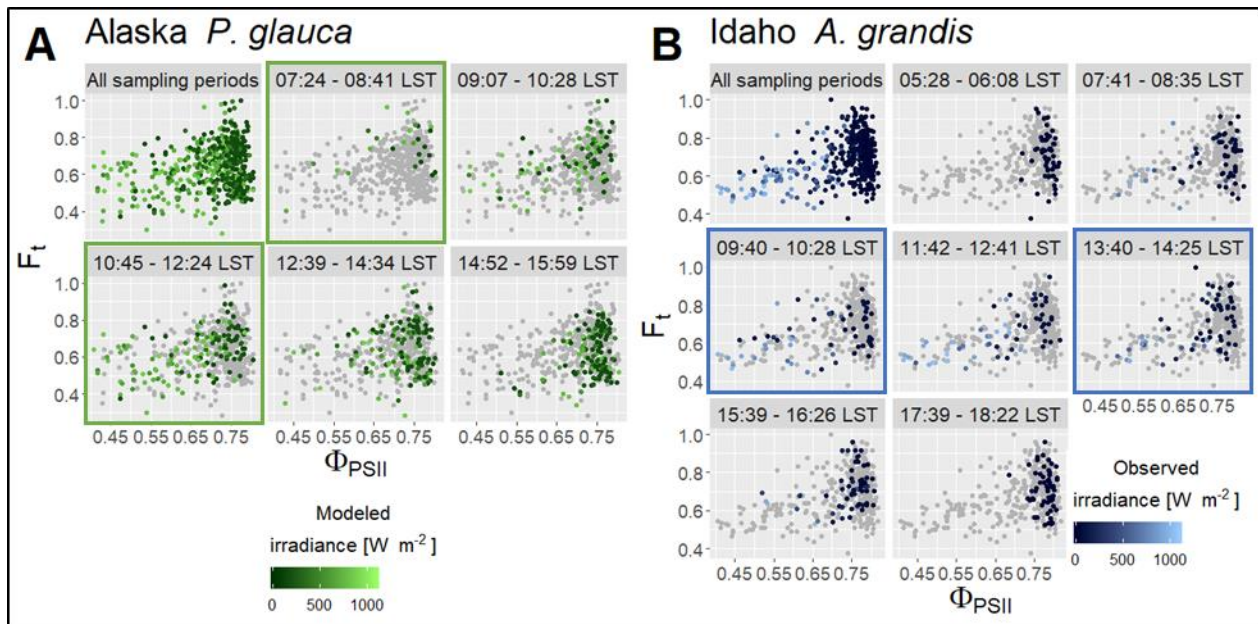


Figure 2. Relationship between steady-state fluorescence yield (F_t) and photosystem II yield (Φ_{PSII}) for *P. glauca* needles in Alaska (A; $n = 523$) and for *A. grandis* needles in Idaho (B; $n = 417$). Modeled (A) and observed (B) irradiance is indicated by coloration of points; grey points in individual sampling period panels (in local solar time, LST) show observations from other periods. Plots of sampling periods most closely aligned with timing of satellite overpasses (e.g., GOME-2 at 09:30 LST and TROPOMI at 13:30 LST) are outlined in colored boxes. Observations of F_t were normalized to $F_{t,max}$ following Magney et al. (2017).

3.3 Empirical support for (bias of) linear SIF—GPP observations

Binning observations of Φ_{PSII} and F_t by temporal sampling windows, including those closely aligned with current satellite overpass times (e.g., GOME-2 and SCHIAMACHY at 09:30 local solar time (LST); GOSAT-2, OCO-2, and TROPOMI at 13:30 LST; see colored boxes outlining select plots, **Fig. 2**), provides field-based visual evidence for observed linearity between spaceborne ‘snapshots’ of SIF and GPP. However, pooling observations across sampling periods suggests that this linear relationship is not universal; rather, SIF retrievals represent aggregated illumination conditions and hence a composite of NPQ- and PQ-limitation that are biased toward top-of-canopy. Despite our evidence that PQ-limitation occurs during all sampling periods (**Fig. 2**) ‘snapshot’ observations often fail to document the decline in F_t at which this breakpoint occurs (van der Tol et al., 2014; Yang et al., 2015). This may be driven by the discrepancy in the range of Φ_{PSII} values associated with NPQ-limitation relative to that of PQ-limitation. Despite this compressed range of variability, 40% and 55% of observations from Alaska and Idaho, respectively, were PQ-limited. Therefore, current spaceborne SIF retrievals, biased toward top-of-canopy, have limited capacity to detect the nuances of sub-canopy responses.

Fortunately, the recently launched OCO-3 instrument follows a precessing orbit, enabling comparison of SIF dynamics across diurnal retrievals. OCO-3 takes up to 70 days to fully capture diurnal variation in SIF for a given location, meaning diurnal variation will be entangled with seasonal variation (Eldering et al., 2019). A forthcoming NASA mission, the geostationary

337 GeoCARB, will further enhance the temporal sampling advancements of OCO-3 by enabling
 338 diurnal observation of SIF at very high temporal resolution (2-3 hours) (Moore III et al., 2018).
 339 GeoCARB will enable rapid assessment of how linearity in the SIF—GPP relationship might
 340 diverge on diurnal and seasonal time-scales.

341

342 3.4 Employing irradiance dependence to predict relative Φ_{PSII} from ChlF

343

344

345

346

347

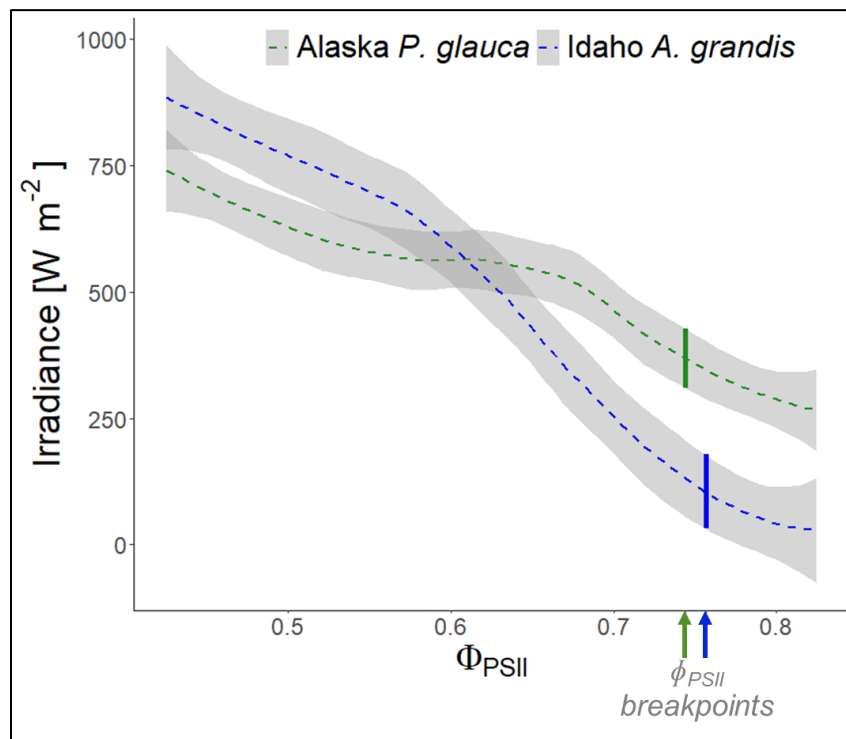
348

349

350

We fit smoothed curves using the loess function in R (R Core Team, 2017) through irradiance data (displayed in **Fig. 2**) binned at 0.05 intervals of Φ_{PSII} to approximate irradiance at the breakpoint in the F_t — Φ_{PSII} relationship (displayed in **Fig. 1**). Irradiance at the breakpoint was greater at the Alaska site (*P. glauca*; mean: 368 W m^{-2} ; 95% confidence interval 310 – 426 W m^{-2}) than at the Idaho site (*A. grandis*; mean: 104 W m^{-2} ; 95% confidence interval 33 – 178 W m^{-2}), respectively (**Fig. 3**). This discrepancy may be related to the means of estimating irradiance or in differences in activation of reversible NPQ (Magney, Bowling, et al., 2019; Raczka et al., 2019).

351



352

353

354

355

356

357

358

359

360

361

362

363

Figure 3. Distribution of modeled (Alaska *P. glauca*) and observed irradiance (Idaho *A. grandis*) by photosystem II yield (Φ_{PSII}) fit with smoothed curves and 95% confidence intervals using the loess function (R Core Team, 2017). Irradiance values are indicated associated with the respective breakpoints in fitted GAMs (see **Fig. 1**).

We used generalized linear models informed by irradiance alone to predict whether a given ChlF observation fell on the NPQ-limited or PQ-limited side of the breakpoint. This approach correctly assigned 70% and 80% of the observations from Alaska and Idaho, respectively. This approach correctly classified observations from Alaska as NPQ-limited more frequently than PQ-limited (78% and 57%, respectively), whereas the opposite was true for Idaho (60% and 97%, respectively). Modeled irradiance from Idaho correctly classified observations as NPQ-limited and as PQ-limited (25% and 86%, respectively, for an overall

364 accuracy of 59%) less frequently than observed irradiance. These findings underscore the
365 challenge of accurately estimating irradiance from canopy structure-informed modeling and the
366 need for more detailed approaches to model within-canopy irradiance for complex canopies.
367 Furthermore, our analyses suggest that whereas shaded foliage is likely PQ-limited – as expected
368 – photochemistry of sunlit foliage may be governed by factors beyond irradiance (e.g., leaf
369 temperature, vapor pressure deficit, soil conditions), which in turn affect NPQ (Baker, 2008;
370 Damm et al., 2010; Maxwell & Johnson, 2000; van der Tol et al., 2014).

371

372 3.5 Implications for remotely sensing Φ_{PSII} from SIF over complex canopies

373

374 Studies linking tower-based SIF observations with contemporaneous leaf-scale PAM
375 fluorescence measurements show promise for remotely sensing canopy physiological status
376 (Magney, Bowling, et al., 2019; Magney, Frankenberg, et al., 2019; Raczka et al., 2019).
377 Mechanistically understanding ChlF across scales of time and space (Magney et al., 2017) and
378 over structurally complex canopies remains a scientific frontier (Nichol et al., 2019). Our results
379 provide field-based evidence to complement findings from remote sensing-based studies that
380 physiological regulation is particularly important for interpreting SIF at the landscape-scale over
381 ENFs (e.g., Walther et al., 2016). Fine-scale heterogeneity in canopy irradiance strongly drives
382 ChlF (Frankenberg & Berry, 2018) and recent studies suggest that accounting for irradiance may
383 improve SIF-based modelling of seasonal variation in sustained NPQ in ENFs (Parazoo et al.,
384 2020; Raczka et al., 2019). We provide an approach to parameterize radiative transfer models
385 (e.g., SCOPE) with information on leaf-level physiology to improve performance of SIF-based
386 terrestrial biosphere models (Parazoo et al., 2020). To determine the generality of this
387 relationship and its application to interpreting large-scale SIF observations, future studies should
388 evaluate how the shapes of the F_t – Φ_{PSII} and SIF–GPP relationships change across ecologically
389 meaningful scales (e.g., crown, canopy or landscape) and seasons and for different species.
390 Furthermore, studies examining SIF should be mindful that, mechanistically, its linkage to
391 photosynthesis is limited to the light reactions and APAR.

391

392 Our findings raise several important questions: (i) given the prominence of PQ-limited,
393 low irradiance observations at the needle-scale, how common is this constraint at the canopy-
394 scale?; (ii) when integrating ChlF emission (e.g., from spaceborne SIF retrievals) of a canopy
395 subject to dynamic, variegated illumination, do equal-area sub-canopy fractions of PQ- or NPQ-
396 limited foliage impose the same weight on the overall SIF yield signal?; and (iii) to what degree
397 are the accuracy of TBMs affected by the propagation of error associated with failing to account
398 for the composition of NPQ- and PQ-limitation in observed SIF?

398

399 **Acknowledgments**

400

401 This research was supported by NASA FINESST grant 80NSSC19K1341 to AJM,
402 NASA ABoVE grant NNX15AT86A to JUHE, LAV, NTB, and KLG, and USDA McIntire-
403 Stennis grant 1018044 to JUHE. We thank the Nokes family for granting us access to the Herald
404 Nokes Family Experimental Forest. We also thank Carlos A. Silva for contributions in
405 processing the airborne lidar data. Algorithms for interpolating DSMs were adapted from
406 programs written by Heather E. Greaves (Greaves et al., 2015, 2016). We thank Johanna E.
407 Jensen for valuable discussions through this project. Fluorescence and irradiance data used in
408 this research may be accessed from the Oak Ridge National Laboratory Distributed Active
409 Archive Center (Maguire et al., 2020).

409

410 **References**

- 411 Akima, H., Gebhardt, A., Petzold, T., & Maechler, M. (2016). Package “akima.” Retrieved from
412 <http://cran.r-project.org/package=akima>
- 413 Alonso, L., Van Wittenberghe, S., Amorós-López, J., Vila-Francés, J., Gómez-Chova, L., &
414 Moreno, J. (2017). Diurnal cycle relationships between passive fluorescence, PRI and NPQ
415 of vegetation in a controlled stress experiment. *Remote Sensing*, 9(8).
416 <https://doi.org/10.3390/rs9080770>
- 417 Baker, N. R. (2008). Chlorophyll Fluorescence: A Probe of Photosynthesis In Vivo. *Annual*
418 *Review of Plant Biology*, 59(1), 89–113.
419 <https://doi.org/10.1146/annurev.arplant.59.032607.092759>
- 420 Bates, D., Maechler, M., Bolker, B., Walker, S., Christensen, R. H. B., Singmann, H., et al.
421 (2018). Package “lme4.” *R Topics Documented*. <https://doi.org/10.2307/2533043>>
- 422 Burnham, K. P., & Anderson, D. R. (2002). *Model Selection and Inference: A practical*
423 *information-theoretic approach* (2nd ed.). New York: Springer-Verlag.
- 424 Celesti, M., van der Tol, C., Cogliati, S., Panigada, C., Yang, P., Pinto, F., et al. (2018).
425 Exploring the physiological information of Sun-induced chlorophyll fluorescence through
426 radiative transfer model inversion. *Remote Sensing of Environment*, 215, 97–108.
427 <https://doi.org/10.1016/j.rse.2018.05.013>
- 428 Corripio, J. G. (2003). Vectorial algebra algorithms for calculating terrain parameters from
429 DEMs and solar radiation modelling in mountainous terrain. *International Journal of*
430 *Geographical Information Science*, 17(1), 1–23. <https://doi.org/10.1080/713811744>
- 431 Corripio, J. G. (2015). Package ‘insol.’
- 432 Damm, A., Elber, J., Erler, A., Gioli, B., Hamdi, K., Hutjes, R., et al. (2010). Remote sensing of
433 sun-induced fluorescence to improve modeling of diurnal courses of gross primary
434 production (GPP). *Global Change Biology*, 16(1), 171–186. <https://doi.org/10.1111/j.1365-2486.2009.01908.x>
- 435
- 436 Eldering, A., Taylor, T. E., O’Dell, C. W., & Pavlick, R. (2019). The OCO-3 mission:
437 measurement objectives and expected performance based on 1 year of simulated data.
438 *Atmospheric Measurement Techniques*, 12(4), 2341–2370. <https://doi.org/10.5194/amt-12-2341-2019>
- 439
- 440 Frankenberg, C., & Berry, J. (2018). Solar Induced Chlorophyll Fluorescence: Origins, Relation
441 to Photosynthesis and Retrieval. In *Comprehensive Remote Sensing* (pp. 143–162). Elsevier.
442 <https://doi.org/10.1016/B978-0-12-409548-9.10632-3>
- 443 Gamache, I., & Payette, S. (2004). Height Growth Response of Tree Line Black Spruce to
444 Recent Climate Warming across the Forest-Tundra of Eastern Canada. *Journal of Ecology*,
445 92(5), 835–845.
- 446 Genty, B., Briantais, J.-M., & Baker, N. R. (1989). The relationship between the quantum yield
447 of photosynthetic electron transport and quenching of chlorophyll fluorescence. *Biochimica*
448 *et Biophysica Acta (BBA) - General Subjects*, 990(1), 87–92. [https://doi.org/10.1016/S0304-4165\(89\)80016-9](https://doi.org/10.1016/S0304-4165(89)80016-9)
- 449
- 450 Greaves, H. E., Vierling, L. A., Eitel, J. U. H., Boelman, N. T., Magney, T. S., Prager, C. M., &
451 Griffin, K. L. (2015). Estimating aboveground biomass and leaf area of low-stature Arctic
452 shrubs with terrestrial LiDAR. *Remote Sensing of Environment*, 164, 26–35.
453 <https://doi.org/10.1016/j.rse.2015.02.023>

- 454 Greaves, H. E., Vierling, L. A., Eitel, J. U. H., Boelman, N. T., Magney, T. S., Prager, C. M., &
455 Griffin, K. L. (2016). High-resolution mapping of aboveground shrub biomass in Arctic
456 tundra using airborne lidar and imagery. *Remote Sensing of Environment*, *184*, 361–373.
457 <https://doi.org/10.1016/j.rse.2016.07.026>
- 458 Gu, L., Han, J., Wood, J. D., Chang, C. Y. Y., & Sun, Y. (2019). Sun- induced Chl fluorescence
459 and its importance for biophysical modeling of photosynthesis based on light reactions. *New*
460 *Phytologist*, *223*(3), 1179–1191. <https://doi.org/10.1111/nph.15796>
- 461 Guanter, L., Zhang, Y., Jung, M., Joiner, J., Voigt, M., Berry, J. A., et al. (2014). Global and
462 time-resolved monitoring of crop photosynthesis with chlorophyll fluorescence.
463 *Proceedings of the National Academy of Sciences*, *111*(14), E1327–E1333.
464 <https://doi.org/10.1073/pnas.1320008111>
- 465 Hall, F. G., Hilker, T., Coops, N. C., Lyapustin, A., Huemmrich, K. F., Middleton, E., et al.
466 (2008). Multi-angle remote sensing of forest light use efficiency by observing PRI variation
467 with canopy shadow fraction. *Remote Sensing of Environment*, *112*(7), 3201–3211.
468 <https://doi.org/10.1016/j.rse.2008.03.015>
- 469 Hilker, T., Coops, N. C., Schwalm, C. R., Jassal, R. S., Black, T. A., & Krishnan, P. (2008).
470 Effects of mutual shading of tree crowns on prediction of photosynthetic light-use
471 efficiency in a coastal Douglas-fir forest. *Tree Physiology*, *28*(6), 825–834.
472 <https://doi.org/10.1093/treephys/28.6.825>
- 473 Hilker, T., Coops, N. C., Hall, F. G., Black, T. A., Wulder, M. a., Nestic, Z., & Krishnan, P.
474 (2008). Separating physiologically and directionally induced changes in PRI using BRDF
475 models. *Remote Sensing of Environment*, *112*(6), 2777–2788.
476 <https://doi.org/10.1016/j.rse.2008.01.011>
- 477 Hilker, T., Hall, F. G., Coops, N. C., Lyapustin, A., Wang, Y., Nestic, Z., et al. (2010). Remote
478 sensing of photosynthetic light-use efficiency across two forested biomes: Spatial scaling.
479 *Remote Sensing of Environment*, *114*(12), 2863–2874.
480 <https://doi.org/10.1016/j.rse.2010.07.004>
- 481 Hilker, T., Coops, N. C., Hall, F. G., Nichol, C. J., Lyapustin, A., Black, T. A., et al. (2011).
482 Inferring terrestrial photosynthetic light use efficiency of temperate ecosystems from space.
483 *Journal of Geophysical Research: Biogeosciences*, *116*(3), 1–11.
484 <https://doi.org/10.1029/2011JG001692>
- 485 Hubbard, T. D., Koehler, R. D., & Combellick, R. A. (2011). High-resolution lidar data for
486 Alaska infrastructure corridors. Alaska Division of Geological & Geophysical Surveys.
487 <https://doi.org/http://doi.org/10.14509/22722>
- 488 Jeong, S. J., Schimel, D., Frankenberg, C., Drewry, D. T., Fisher, J. B., Verma, M., et al. (2017).
489 Application of satellite solar-induced chlorophyll fluorescence to understanding large-scale
490 variations in vegetation phenology and function over northern high latitude forests. *Remote*
491 *Sensing of Environment*, *190*, 178–187. <https://doi.org/10.1016/j.rse.2016.11.021>
- 492 Krause, G. H., & Weis, E. (1991). Chlorophyll Fluorescence and Photosynthesis: The Basics.
493 *Annual Review of Plant Physiology and Plant Molecular Biology*, *42*(1), 313–349.
494 <https://doi.org/10.1146/annurev.pp.42.060191.001525>
- 495 Levelt, P. F., van den Oord, G. H. J., Dobber, M. R., Mälkki, A., Visser, H., de Vries, J., et al.
496 (2006). The ozone monitoring instrument. *IEEE Transactions on Geoscience and Remote*
497 *Sensing*, *44*(5), 1093–1101. Retrieved from
498 <http://ieeexplore.ieee.org/lpdocs/epic03/wrapper.htm?arnumber=1624601>
- 499 Li, Xiaowen, & Strahler, A. H. (1985). Geometric-Optical Bidirectional Reflectance Modeling of

- 500 a Conifer Forest Canopy. *IEEE Transactions on Geoscience and Remote Sensing*, *GE-*
501 *24*(5), 705–721. <https://doi.org/10.1109/TGRS.1986.289706>
- 502 Li, Xing, Xiao, J., He, B., Altaf Arain, M., Beringer, J., Desai, A. R., et al. (2018). Solar-induced
503 chlorophyll fluorescence is strongly correlated with terrestrial photosynthesis for a wide
504 variety of biomes: First global analysis based on OCO-2 and flux tower observations.
505 *Global Change Biology*, *24*(9), 3990–4008. <https://doi.org/10.1111/gcb.14297>
- 506 Magney, T. S., Frankenberg, C., Fisher, J. B., Sun, Y., North, G. B., Davis, T. S., et al. (2017).
507 Connecting active to passive fluorescence with photosynthesis: a method for evaluating
508 remote sensing measurements of Chl fluorescence. *New Phytologist*, *215*(4), 1594–1608.
509 <https://doi.org/10.1111/nph.14662>
- 510 Magney, T. S., Frankenberg, C., Köhler, P., North, G., Davis, T. S., Dold, C., et al. (2019).
511 Disentangling changes in the spectral shape of chlorophyll fluorescence: Implications for
512 remote sensing of photosynthesis. *Journal of Geophysical Research: Biogeosciences*,
513 2019JG005029. <https://doi.org/10.1029/2019JG005029>
- 514 Magney, T. S., Bowling, D. R., Logan, B. A., Grossmann, K., Stutz, J., Blanken, P. D., et al.
515 (2019). Mechanistic evidence for tracking the seasonality of photosynthesis with solar-
516 induced fluorescence. *Proceedings of the National Academy of Sciences*, *116*(24), 11640–
517 11645. <https://doi.org/10.1073/pnas.1900278116>
- 518 Maguire, A. J., Eitel, J. U. H., Griffin, K. L., Schmiege, S. C., Bruner, S. G., Boelman, N. T., &
519 Weygint, W. A. (2020). Needle-level chlorophyll fluorescence and irradiance, AK and ID,
520 2017-2019. Oak Ridge, Tennessee, USA: ORNL DAAC.
521 <https://doi.org/https://doi.org/10.3334/ORNLDAAC/1785>
- 522 Maxwell, K., & Johnson, G. N. (2000). Chlorophyll fluorescence -- a practical guide. *Journal of*
523 *Experimental Botany*, *51*(345), 659–668. <https://doi.org/10.1093/jexbot/51.345.659>
- 524 Mesinger, F., DiMego, G., Kalnay, E., Mitchell, K., Shafran, P. C., Ebisuzaki, W., et al. (2006).
525 North American Regional Reanalysis. *Bulletin of the American Meteorological Society*,
526 *87*(3), 343–360. <https://doi.org/10.1175/BAMS-87-3-343>
- 527 Middleton, E. M., Cheng, Y. Ben, Hilker, T., Black, T. A., Krishnan, P., Coops, N. C., &
528 Huemmrich, K. F. (2009). Linking foliage spectral responses to canopy-level ecosystem
529 photosynthetic light-use efficiency at a douglas-fir forest in Canada. *Canadian Journal of*
530 *Remote Sensing*, *35*(2), 166–188. <https://doi.org/10.5589/m09-008>
- 531 Moore III, B., Crowell, S. M. R., Rayner, P. J., Kumer, J., O'Dell, C. W., O'Brien, D., et al.
532 (2018). The Potential of the Geostationary Carbon Cycle Observatory (GeoCarb) to Provide
533 Multi-scale Constraints on the Carbon Cycle in the Americas. *Frontiers in Environmental*
534 *Science*, *6*(OCT), 1–13. <https://doi.org/10.3389/fenvs.2018.00109>
- 535 Nakagawa, S., & Schielzeth, H. (2013). A general and simple method for obtaining R2 from
536 generalized linear mixed-effects models. *Methods in Ecology and Evolution*, *4*(2), 133–142.
537 <https://doi.org/10.1111/j.2041-210x.2012.00261.x>
- 538 Nichol, C. J., Drolet, G., Porcar-Castell, A., Wade, T., Sabater, N., Middleton, E. M., et al.
539 (2019). Diurnal and Seasonal Solar Induced Chlorophyll Fluorescence and Photosynthesis
540 in a Boreal Scots Pine Canopy. *Remote Sensing*, *11*(3), 273.
541 <https://doi.org/10.3390/rs11030273>
- 542 Parazoo, N. C., Frankenberg, C., Köhler, P., Joiner, J., Yoshida, Y., Magney, T., et al. (2019).
543 Towards a Harmonized Long- Term Spaceborne Record of Far- Red Solar- Induced
544 Fluorescence. *Journal of Geophysical Research: Biogeosciences*, 2019JG005289.
545 <https://doi.org/10.1029/2019JG005289>

- 546 Parazoo, N. C., Magney, T. S., Norton, A., Raczka, B., Bacour, C., Maignan, F., et al. (2020).
547 Wide discrepancies in the magnitude and direction of modelled SIF in response to light
548 conditions. *Biogeosciences*, (February), 1–42. <https://doi.org/10.5194/bg-2019-508>
- 549 Porcar-Castell, A., Bäck, J., Juurola, E., & Hari, P. (2006). Dynamics of the energy flow through
550 photosystem II under changing light conditions: a model approach. *Functional Plant*
551 *Biology*, 33(3), 229. <https://doi.org/10.1071/FP05133>
- 552 Porcar-Castell, A., Pfündel, E., Korhonen, J. F. J., & Juurola, E. (2008). A new monitoring PAM
553 fluorometer (MONI-PAM) to study the short- and long-term acclimation of photosystem II
554 in field conditions. *Photosynthesis Research*, 96(2), 173–179.
555 <https://doi.org/10.1007/s11120-008-9292-3>
- 556 Porcar-Castell, A., Tyystjärvi, E., Atherton, J., van der Tol, C., Flexas, J., Pfündel, E. E., et al.
557 (2014). Linking chlorophyll a fluorescence to photosynthesis for remote sensing
558 applications: Mechanisms and challenges. *Journal of Experimental Botany*, 65(15), 4065–
559 4095. <https://doi.org/10.1093/jxb/eru191>
- 560 R Core Team. (2017). R: A language and environment for statistical computing. Vienna, Austria:
561 R Foundation for Statistical Computing. Retrieved from <https://www.r-project.org>
- 562 Raczka, B., Porcar- Castell, A., Magney, T., Lee, J. E., Köhler, P., Frankenberg, C., et al.
563 (2019). Sustained Nonphotochemical Quenching Shapes the Seasonal Pattern of Solar-
564 Induced Fluorescence at a High- Elevation Evergreen Forest. *Journal of Geophysical*
565 *Research: Biogeosciences*, 124(7), 2005–2020. <https://doi.org/10.1029/2018JG004883>
- 566 Roussel, J.-R., Auty, D., De Boissieu, F., & Meador, A. S. (2017). Package ‘lidR.’
- 567 Silva, C. A., Crookston, N. L., Hudak, A. T., Vierling, L. A., Klauberg, C., & Cardil, A. (2017).
568 Package ‘rLiDAR.’
- 569 Sun, Y., Frankenberg, C., Wood, J. D., Schimel, D. S., Jung, M., Guanter, L., et al. (2017).
570 OCO-2 advances photosynthesis observation from space via solar-induced chlorophyll
571 fluorescence. *Science*, 358(6360), eaam5747. <https://doi.org/10.1126/science.aam5747>
- 572 van der Tol, C., Verhoef, W., & Rosema, A. (2009). A model for chlorophyll fluorescence and
573 photosynthesis at leaf scale. *Agricultural and Forest Meteorology*, 149(1), 96–105.
574 <https://doi.org/10.1016/j.agrformet.2008.07.007>
- 575 van der Tol, C., Verhoef, W., Timmermans, J., Verhoef, A., & Su, Z. (2009). An integrated
576 model of soil-canopy spectral radiances, photosynthesis, fluorescence, temperature and
577 energy balance. *Biogeosciences*, 6, 3109–3129. Retrieved from
578 [http://getitatduke.library.duke.edu/?&url_ver=Z39.88-
579 2004&url_ctx_fmt=info:ofi/fmt:kev:mtx:ctx&rft_val_fmt=info:ofi/fmt:kev:mtx:journal&rft.
580 atitle=An integrated model of soil-canopy spectral radiances%2C photosynthesis%2C
581 fluorescence%2C temperature and e](http://getitatduke.library.duke.edu/?&url_ver=Z39.88-2004&url_ctx_fmt=info:ofi/fmt:kev:mtx:ctx&rft_val_fmt=info:ofi/fmt:kev:mtx:journal&rft.atitle=An%20integrated%20model%20of%20soil-canopy%20spectral%20radiance%20photosynthesis%20fluorescence%20temperature%20and%20energy%20balance)
- 582 van der Tol, C., Berry, J. A., Campbell, P. K. E., & Rascher, U. (2014). Models of fluorescence
583 and photosynthesis for interpreting measurements of solar-induced chlorophyll
584 fluorescence. *Journal of Geophysical Research: Biogeosciences*, 119(12), 2312–2327.
585 <https://doi.org/10.1002/2014JG002713>. We
- 586 Walther, S., Voigt, M., Thum, T., Gonsamo, A., Zhang, Y., Köhler, P., et al. (2016). Satellite
587 chlorophyll fluorescence measurements reveal large-scale decoupling of photosynthesis and
588 greenness dynamics in boreal evergreen forests. *Global Change Biology*, 22(9), 2979–2996.
589 <https://doi.org/10.1111/gcb.13200>
- 590 Wen, J., Köhler, P., Duveiller, G., Parazoo, N. C., Magney, T. S., Hooker, G., et al. (2020). A
591 framework for harmonizing multiple satellite instruments to generate a long-term global

592 high spatial-resolution solar-induced chlorophyll fluorescence (SIF). *Remote Sensing of*
593 *Environment*, 239(December 2019), 111644. <https://doi.org/10.1016/j.rse.2020.111644>
594 Wieneke, S., Burkart, A., Cendrero-Mateo, M. P., Julitta, T., Rossini, M., Schickling, A., et al.
595 (2018). Linking photosynthesis and sun-induced fluorescence at sub-daily to seasonal
596 scales. *Remote Sensing of Environment*, 219(September), 247–258.
597 <https://doi.org/10.1016/j.rse.2018.10.019>
598 Wood, S. N. (2019). Package “mgcv.”
599 Yang, X., Tang, J., Mustard, J. F., Lee, J.-E., Rossini, M., Joiner, J., et al. (2015). Solar-induced
600 chlorophyll fluorescence that correlates with canopy photosynthesis on diurnal and seasonal
601 scales in a temperate deciduous forest. *Geophysical Research Letters*, 42(8), 2977–2987.
602 <https://doi.org/10.1002/2015GL063201>
603